

Realizing Surface-Driven Flows in the Primitive Equations

ERIC BEMBENEK, FRANCIS J. POULIN, AND MICHAEL L. WAITE

Department of Applied Mathematics, University of Waterloo, Waterloo, Ontario, Canada

(Manuscript received 14 May 2014, in final form 25 February 2015)

ABSTRACT

The surface quasigeostrophic (SQG) model describes flows with surface buoyancy perturbations with no interior quasigeostrophic potential vorticity at small Rossby number Ro and $O(1)$ Burger number, where quasigeostrophic dynamics are expected to hold. Numerical simulations of SQG dynamics have shown that vortices are frequently generated at small scales, which may have $O(1)$ Rossby numbers and therefore may be beyond the limits of SQG. This paper examines the dynamics of an initially geostrophically balanced elliptical surface buoyancy perturbation in both the SQG model and the nonhydrostatic Boussinesq primitive equations (PE). In the case of very small Rossby number, it is confirmed that both models agree, as expected. For larger Ro , non-SQG effects emerge and as a result the solution of the PE deviates significantly from that of SQG. In particular, an increase in the Rossby number has the following effects: (i) the buoyancy filaments at the surface are stabilized in that they generate fewer secondary vortices; (ii) the core of the vortex experiences inertial instability, which results in a uniform buoyancy profile in its interior; (iii) the divergent part of the energy spectrum increases in magnitude; (iv) the PE model has significantly more gravity waves that are radiated from the vortex; (v) the magnitude of the vertical velocity increases; and (vi) in the mature stages of evolution, there are gravitational instabilities that develop because of the complicated dynamics inside the vortex. It is demonstrated that significant non-SQG effects are evident when the large-scale Rossby number of the initial flow is about 0.05 and the local Rossby number is $O(1)$.

1. Introduction

The surface quasigeostrophic (SQG) model describes large-scale (mesoscale) ocean and atmospheric dynamics that are driven by the advection of surface buoyancy anomalies near boundaries in the vertical. The model is derived from the Boussinesq equations through an asymptotic expansion with the assumption of a small Rossby number and $O(1)$ Burger number (e.g., Juckes 1994; Held et al. 1995; Vallis 2006). An interesting characteristic of this model is that it generates small-scale structures that do not necessarily have a small Rossby number associated with them and therefore could be beyond the limits of the model (e.g., see Juckes 1994; Held et al. 1995). This is a well-known limitation of the SQG model (Held et al. 1995). To better understand these limitations, we investigate how SQG dynamics manifest themselves in the full nonhydrostatic

Boussinesq primitive equations (PE), a model that is able to accurately describe a much wider range of motions.

The SQG model has been successfully applied to mesoscale ocean dynamics (e.g., Lapeyre and Klein 2006; LaCasce and Mahadevan 2006) and also the atmosphere (e.g., Tulloch and Smith 2006, 2009). It has been demonstrated that SQG model results agree well with observational data under certain conditions. For example, Le Traon et al. (2008) argued that SQG dynamics yield a kinetic energy spectrum that is closer to the wavenumber spectra observed in the Gulf Stream, the Kuroshio, and the Agulhas regions compared to quasigeostrophic (QG) theory. Tulloch and Smith (2006) used a finite-depth SQG model to generate a $-5/3$ atmospheric mesoscale energy spectrum and a -3 spectrum at larger scales, in agreement with observations around the tropopause (e.g., Nastrom and Gage 1985).

Even though SQG assumes zero quasigeostrophic potential vorticity (QGPV) in the interior, Lapeyre and Klein (2006) showed that their “effective SQG” model agreed quite well with flows that contain an SQG layer and both a barotropic and first baroclinic mode of QGPV. Their model was consistent with observations

Corresponding author address: Eric Bembenek, Department of Applied Mathematics, University of Waterloo, 200 University Avenue West, Waterloo ON N2L 3G1, Canada.
E-mail: abembene@uwaterloo.ca

for dynamics near the surface; however, it failed to accurately describe the dynamics far enough away from the surface. While the assumption of zero interior QGPV is artificial, it is a convenient choice that leads to a much simpler model than the general case and, as a result, it is often made (e.g., Held et al. 1995; Tulloch and Smith 2006; LaCasce 2012).

In this article, we compare the dynamics generated from the SQG model with a PE model that does not assume an infinitesimal Rossby number and therefore should be more accurate in describing a wider range of geophysical flows. This comparison aims to determine the parameter regimes in which the SQG equations are valid and the type of non-SQG dynamics that occur outside this regime. While other works have considered realizations of SQG dynamics in the PE (e.g., Lapeyre and Klein 2006; Klein et al. 2008; Danioux et al. 2012), our study is based on an exploration of how the dynamics vary with the Rossby number, while previous studies have focused on one value of the Rossby number. We investigate the particular case of an elliptical vortex of surface buoyancy perturbation. The evolution of elliptical vortices has been well studied (e.g., Held et al. 1995; Carton 2009; Dritschel 2011). Held et al. (1995) chose this idealized case as the first example in their presentation of SQG. Carton (2009) analyzed the instabilities of elliptical vortices and demonstrated how SQG dynamics differ from two-dimensional barotropic flow. Dritschel (2011) studied instabilities of elliptical vortices in the limit of vanishing thickness of an ellipsoid. Snyder et al. (2007) studied an SQG vortex dipole in the PE and showed that inertia–gravity waves are generated during the early stages of the PE simulations due to initial adjustment. Further, the study showed that gravity waves can be spontaneously generated at later stages of the simulation. While the study in Snyder et al. (2007) follows a similar approach to what we present here, it is significantly different in that they studied a vortex dipole that is a steady-state solution to the SQG model. Our choice of initial condition is not steady and develops long, narrow filaments that are unstable and subsequently generate secondary vortices. Several other studies have also compared the QG model to the PE (e.g., Whitaker 1993; Frisius 2003; Molemaker et al. 2010). Whitaker (1993) compared the results of a two-layer QG model to the corresponding analog for a PE model. Frisius (2003) studied the cyclone–anticyclone asymmetry in the hydrostatic Boussinesq equations against the QG model. Molemaker et al. (2010) discussed routes to energy dissipation in a forced turbulent flow in the QG model and PE in the context of the forced dissipative Eady problem.

This article is structured as follows: In section 2, we give a review of the Boussinesq approximation along

with the QG equations. Section 3 describes the numerical methods used to integrate a nonhydrostatic Boussinesq fluid and the numerical methods that solve the SQG model. Section 4 gives an analysis on the numerical results. Finally, section 5 concludes our findings.

2. Mathematical models for the oceans and atmosphere

a. The Boussinesq model

The nonhydrostatic Boussinesq PE are a set of equations that describe a wide range of fluid motion with small density variations (e.g., Vallis 2006; Kundu and Cohen 2010). The Boussinesq approximation is very accurate in describing most large-scale oceanic dynamics and is also applicable to shallow atmospheric motions as well. The governing equations consist of the momentum, thermodynamic, and continuity equations:

$$\frac{D\mathbf{u}}{Dt} + \mathbf{f} \times \mathbf{u} = -\frac{1}{\rho_0} \nabla p' + b' \mathbf{k}, \quad (1)$$

$$\frac{Db'}{Dt} + N^2 w = 0, \quad (2)$$

$$\nabla \cdot \mathbf{u} = 0, \quad (3)$$

where ρ_0 , g , $\mathbf{f} = f\mathbf{k}$, and N are the reference density, gravity, Coriolis parameter (which we take as constant throughout), and buoyancy frequency, respectively. Dynamic pressure and density are given by p' and ρ' . Buoyancy perturbations are related to dynamic density as

$$b' = -g \frac{\rho'}{\rho_0}. \quad (4)$$

Finally, \mathbf{u} denotes the three-dimensional velocity field.

Throughout this work, we assume constant buoyancy frequency that allows us to find an exact solution for the vertical structure of the SQG flow. Although this assumption may not be realized in all layers of the oceans or atmosphere, it is commonly made in idealized SQG studies (e.g., Held et al. 1995; Tulloch and Smith 2006). Furthermore, we shall neglect viscosity and diffusion; however, small-scale dissipation is applied via a hyperviscosity filter, which is further described in section 3. Finally, we assume a rigid lid and a flat bottom.

b. The SQG model

Both QG and SQG can be used to describe rapidly rotating, large scale, and relatively slow moving flows (e.g., Held et al. 1995; Vallis 2006). These models are only strictly valid in describing motions that have a small Rossby number:

$$\text{Ro} = \frac{U}{fL}, \quad (5)$$

where U , L are the characteristic velocity and length scales of the flow. The smallness of the Rossby number indicates that the ambient rotation of Earth dominates advection and this leads to geostrophic balance at leading order. Since the velocity is nearly nondivergent in the horizontal, we can introduce a streamfunction ψ which, when combined with hydrostatic balance, yields the diagnostic relationship $b' = f\partial_z\psi$.

Another underlying assumption of QG and SQG is that the horizontal length scale L is of the same order as the Rossby deformation radius L_d :

$$L \sim \frac{NH}{f} = L_d. \quad (6)$$

This assumption of length scales yields the QG equations as opposed to the planetary geostrophy equations that describe synoptic-scale motions in the oceans. When combined, the assumptions of mesoscale motions with small Rossby number imply that the vertical Froude number is small and of the order of the Rossby number:

$$\text{Fr} = \frac{U}{NH} = \text{Ro} \frac{L}{L_d}. \quad (7)$$

The boundary conditions that we impose are a rigid lid at the top of the fluid, a flat bottom below, and periodicity in the horizontal. These assumptions lead to conservation of buoyancy at the surface and bottom:

$$\frac{D_g b'}{Dt} = 0, \quad \text{at } z = 0, -H, \quad (8)$$

where D_g/Dt is the horizontal material derivative with advection due to geostrophic velocities. In the interior, QGPV is conserved following the flow in the horizontal

$$\frac{D_g q}{Dt} = 0 \quad \text{for } -H < z < 0, \quad (9)$$

where q is the QGPV:

$$q = \nabla^2 \psi + \left(\frac{f}{N}\right)^2 \frac{\partial^2 \psi}{\partial z^2}. \quad (10)$$

c. The SQG solution

Solar heating at the surface of Earth warms the ocean from above and heats the atmosphere from below. Both these scenarios can be idealized by SQG dynamics. In this work, we neglect any external forces and instead

study the initial value problem of how a buoyancy anomaly field at the surface of the fluid evolves in space and time. We shall focus on the oceanographic problem, but many of these results apply to the analogous atmospheric problem (e.g., [Tulloch and Smith 2006](#); [Tulloch and Smith 2009](#)).

We begin by assuming a surface buoyancy perturbation given by $b'(z=0) = b^t(x, y)$, where time dependence has been suppressed for clarity. The buoyancy perturbation at the bottom is assumed to be zero: $b'(z=-H) = 0$. The original solution of [Held et al. \(1995\)](#) considered a semi-infinite domain in the vertical, which yielded an exponentially decaying vertical solution for each wavenumber. Since the PE are three-dimensional, we shall assume that the domain has a finite depth (as in [Tulloch and Smith 2006](#)). The QGPV is assumed to be zero everywhere in order to focus on the effects of buoyancy at the surface. Because of the assumption of doubly periodic horizontal boundary conditions, we can decompose the solution in terms of horizontal Fourier modes. This leads to the solution in [Tulloch and Smith \(2006\)](#), in mixed physical-spectral space:

$$\hat{\psi}(k, l, z) = \frac{1}{NK} \frac{\cosh\left[\frac{NK}{f}(z+H)\right]}{\sinh\left(\frac{NKH}{f}\right)} \hat{b}^t(k, l), \quad (11)$$

where $K = \sqrt{k^2 + l^2}$ and k, l are horizontal wavenumbers, and the hat denotes the horizontal Fourier coefficient. Furthermore, the three-dimensional buoyancy field is given by

$$\hat{b}(k, l, z) = \frac{\sinh\left[\frac{NK}{f}(z+H)\right]}{\sinh\left(\frac{NKH}{f}\right)} \hat{b}^t(k, l). \quad (12)$$

From Eqs. (11) and (12), we see that solutions at the surface decay exponentially with an e -folding scale of $f/(NK)$. Hence, small-scale (large K) structures decay faster compared to large-scale structures that have a deeper vertical profile and thus have a stronger influence on motions away from the surface. An interesting aspect of the finite-depth SQG model, described in [Tulloch and Smith \(2006\)](#), is that by varying the Rossby radius, one can find a transition between QG and SQG motion where $KL_d = 1$. Specifically, horizontal structures with length scales larger than L_d behave like QG motion, while length scales smaller than L_d behave like SQG motion. In particular, [Tulloch and Smith \(2006\)](#) showed that large-scale forced turbulence simulations can yield an energy spectrum that has a -3 power law for $KL_d \ll 1$ and a $-5/3$ spectrum for $KL_d \gg 1$. This result, in

addition to the fact that the deepest vertical scale is $fL/2\pi N$, implies that we should take the depth of the domain to be $H = fL/N$, where L is the largest length scale in the initial condition.

3. Numerical approach

To quantify the differences between SQG and the full PE dynamics, it is necessary to employ highly accurate numerical methods to precisely resolve the nonlinear dynamics of the flow. This can be done very efficiently in our doubly periodic domain using Fourier spectral collocation methods (e.g., Hussaini et al. 1989; Boyd 2001). The two dimensional SQG dynamics are solved using QG3, a pseudospectral code (G. R. Flierl 2014, personal communication) with an inverter between streamfunction and PV. Time stepping in QG3 is a third-order Adams–Bashforth method.

To solve the nonhydrostatic PE we use a three-dimensional pseudospectral collocation solver parallelized using a message passing interface (MPI) called the Spectral Parallel Incompressible Navier–Stokes Solver (SPINS) (Subich et al. 2013). In the vertical, we use a Chebyshev grid, and the only boundary conditions that we impose at the top and bottom are those of no normal flow. The vertical grid is clustered near the upper and lower boundaries making this choice advantageous in studying surface-trapped flows. Vertical derivatives are computed using a discrete cosine transform as describe in Trefethen (2000). Fourier transforms are implemented using the Fastest Fourier Transform in the West (FFTW) (Frigo and Johnson 2005). Time stepping is, again, third-order Adams–Bashforth with a fixed time step of 1 min. By contrast, the time step in the SQG simulations is 4.8 min.

Small-scale dissipation in both models is applied with an exponential filter that mimics the effects of a hyperviscosity filter (e.g., Canuto et al. 1988; LaCasce 1998). While QG3 applies this filter radially in spectral space, SPINS applies the filter separately in each direction. The filter has the form

$$s(k) = \exp(-\alpha k^\beta). \quad (13)$$

Parameter values are shown in Table 1. There are three cases that we shall define concretely in section 4b. These parameter values are chosen such that, if $k_{\max} = \pi/\Delta x$, the filter strength corresponds to $s(0.4k_{\max}) = 0.9$ and $s(0.5k_{\max}) = 0.5$. A slightly stronger filter was required in our highest Ro case (see section 4b), where the downscale energy cascade is enhanced; we use $s(0.35k_{\max}) = 0.9$ and $s(0.5k_{\max}) = 0.5$ for the first 2 days of integration. After the first 2 days, we use the filter for the cases with Ro = 0.005 and 0.05.

TABLE 1. Filter parameters used in our numerical simulations with SPINS.

Ro	α	β
0.005	133.79	10.31
0.05	133.79	10.31
0.1 (for first 2 days)	26.64	5.27
0.1 (after first 2 days)	133.79	10.31

4. Results

In this section, we present results of numerical simulations of the SQG and PE models. Both models use identical initial conditions [see Eq. (14) below]. The SQG solver had a runtime of about 10 min on a 512^2 grid that ran in serial on a desktop. On the other hand, the SPINS solver was run on a cluster [Shared Hierarchical Academic Research Computing Network (SHARCNET)] with 64 cores in parallel, and simulations ran for about 3 days on a 512^3 grid. The simulations using SPINS are much slower for two reasons. First, SPINS integrates the PE in three dimensions in contrast to the two-dimensional model in SQG. Second, it is necessary to sufficiently resolve the highest-frequency inertia–gravity waves in order to guarantee numerical stability. The fastest gravity waves have a period of $2\pi/N$. With $N = 10^{-2}\text{s}^{-1}$, the value chosen for all of our simulations, the period is about 10 min. Therefore, in order to properly resolve these gravity waves, we choose a time step of 1 min. The fact that we are using similar methods for both spatial and temporal discretizations and the same number of grid points suggests that the numerical error should be comparable in the two sets of simulations. Therefore, the differences between the two solutions are believed to be because of the underlying dynamics of the SQG and PE models and not because of numerical error. However, the SQG model has no filter applied in the vertical direction, unlike the PE model.

a. SQG solution

The initial condition for the buoyancy perturbation is chosen to be an asymmetric Gaussian profile (Held et al. 1995):

$$b^l(x, y) = b_{\max} \exp \left[-\left(\frac{x}{l/6} \right)^2 - \left(\frac{4y}{l/6} \right)^2 \right], \quad (14)$$

where $l = 200\text{ km}$ and $b_{\max} = 0.01\text{ m s}^{-2}$. This buoyancy results in a maximum horizontal velocity of approximately $U = 0.5\text{ m s}^{-1}$. Other parameters are chosen to be typical values of the upper ocean at midlatitudes: $H = 1\text{ km}$, $N = 10^{-2}\text{ s}^{-1}$, and $f = 10^{-4}\text{ s}^{-1}$. The domain size is $200\text{ km} \times 200\text{ km}$. While SQG does not depend on the Rossby number, we can compute the Rossby number using the maximum horizontal velocity as the characteristic velocity

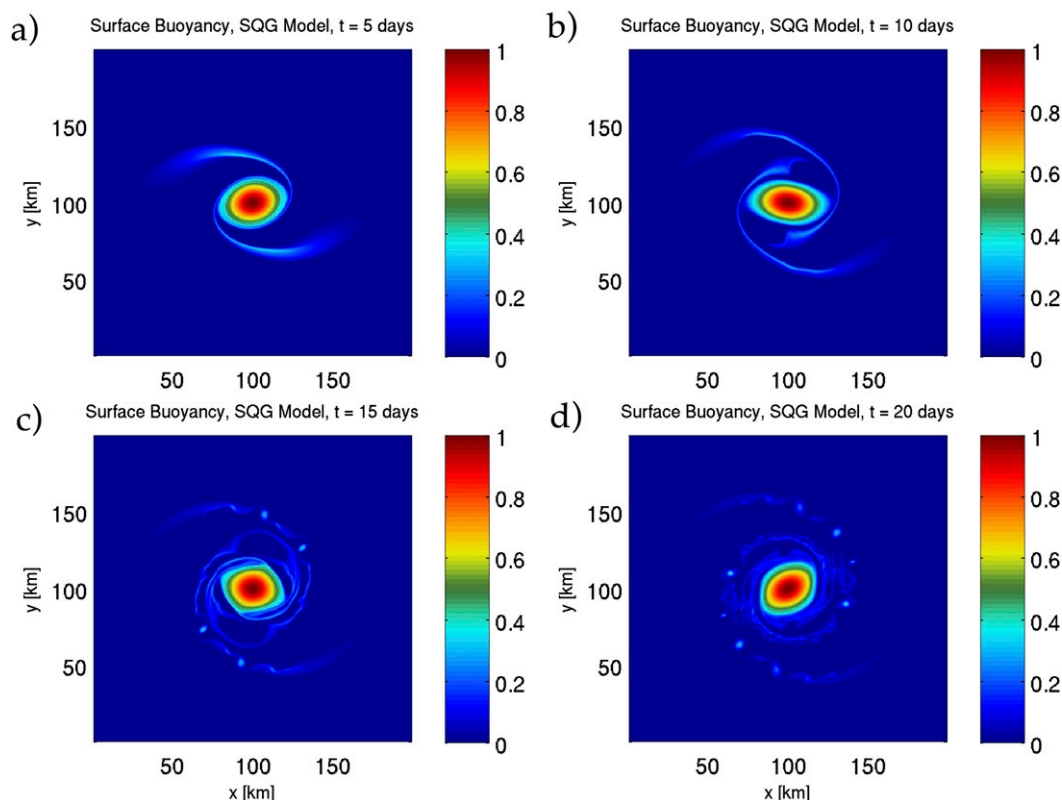


FIG. 1. Surface buoyancy evolution at $t =$ (a) 5, (b) 10, (c) 15, and (d) 20 days in the SQG model. Buoyancy fields are normalized by $b_{\max} = 0.01 \text{ m s}^{-2}$ and are plotted at $z = 0$.

and the semimajor axis of the elliptical vortex as the characteristic length $L = 100 \text{ km}$, as $\text{Ro} = 0.05$. The characteristic length is computed as 4 times the standard deviation of the Gaussian in the x direction, $4\sigma \approx 95 \text{ km}$, which we round to 100 km to get a characteristic length scale.

Figure 1 shows snapshots of the evolution of the surface buoyancy perturbations normalized by $b_{\max} = 0.01 \text{ m s}^{-2}$, found with the SQG model at different times. The vortex rotates anticyclonically and develops filaments in the form of arms that are stretched thinly and eventually become unstable, generating much smaller-scale vortices [as was observed in Held et al. (1995)]. Since this is a solution of the SQG equations, all structures, including the small vortices that develop on the filaments, are strictly SQG regardless of their respective Rossby number. These small-scale vortical structures, which have decreased in scale by a factor of 10–100, should have a Rossby number that is larger by a factor of 10–100 compared to the original vortex. This significant difference in scale raises the question of whether these vortices are still SQG in nature and, if not, how should the flow really be evolving at these scales? To address this question, we look at the evolution of this elliptical vortex in the PE at various Rossby number.

b. PE solutions

The PE are initialized using precisely the same 3D fields as in the SQG model. In particular, the buoyancy field is chosen based on Eq. (12), the horizontal velocity is specified from geostrophic balance, the pressure is calculated from hydrostatic balance, and the vertical velocity is initially zero. For the PE simulations, we shall consider three cases with Rossby numbers: $\text{Ro} = 0.005$, 0.05 , and 0.1 . The parameters used in the three different simulations are stated in Table 2. The characteristic velocity, $U = 0.5 \text{ m s}^{-1}$, and length, $L = 100 \text{ km}$, are fixed between runs. To vary the Rossby number in the simulations of the PE, we change the Coriolis frequency. Looking at Eqs. (11) and (12), we can see that by varying f the e -folding scale of the initial flow changes. To allow for a fair comparison between PE simulations, we shall also change the depth H so that the vertical decay per vertical grid point is the same between the different simulations. In other words, the aspect ratio of the vortex depth to the domain depth is the same in all cases. We choose H to be much larger than the vortex depth to minimize lower boundary effects. Since the time scale of the vortex is L/U but the time step in the PE model is set

TABLE 2. The full set of parameter values for each run in the PE simulations.

Ro	f (s ⁻¹)	H (km)	N (s ⁻¹)	U (m s ⁻¹)	L (km)	min(Δz) (m)	max(Δz) (m)	Δx (m)
0.005	10^{-3}	10	10^{-2}	0.5	100	1.5	120	390
0.05	10^{-4}	1	10^{-2}	0.5	100	0.15	12	390
0.1	5×10^{-5}	0.5	10^{-2}	0.5	100	0.075	6.1	390

by N , we find that by varying f and H , we can run different cases in about the same amount of computational time. This choice of varying parameters can lead to a somewhat unphysical depth, as in $\text{Ro} = 0.005$, $H = 10$ km, which can lead to an unphysical effective sea surface height, approximately 2.5 m in the case with $\text{Ro} = 0.005$. However, we have also simulated the dynamics in the case where $\text{Ro} = 0.005$ with $H = 1$ km and decreasing $U = 0.05$ m s⁻¹ and, after integrating over the first 10 vortex time scales, found excellent agreement between two $\text{Ro} = 0.005$ cases (not shown).

Figure 2 shows snapshots of the surface buoyancy normalized by $b_{\text{max}} = 0.01$ m s⁻² at $t = 10$ days for the SQG model along with the same field for the respective PE runs for the cases with $\text{Ro} = 0.005$, 0.05, and 0.1. As expected, we have excellent agreement between the SQG solution and PE solution at the smallest Rossby

number $\text{Ro} = 0.005$. This indicates that SQG does a very good job of approximating the full PE dynamics when the Rossby number is sufficiently small. Increasing the Rossby number tenfold, the vortex still develops thin arms along with their subsequent destabilization due to the strong shear, very similar to the SQG solution (the destabilization is more apparent at later times; see Fig. 3). By contrast with SQG, however, we see that the core of the vortex diverges horizontally and is more uniform within. This is because the $\text{Ro} = 0.05$ case has negative Ertel PV in the core of the anticyclone and therefore experiences inertial instabilities in the early stages of its evolution (Kloosterziel et al. 2007; see section 4c). When $\text{Ro} = 0.1$, the arms of the vortex still form; however, the instabilities of the filaments do not appear. The core of the vortex, as in the $\text{Ro} = 0.05$ case, is remarkably more spread out compared to the previous

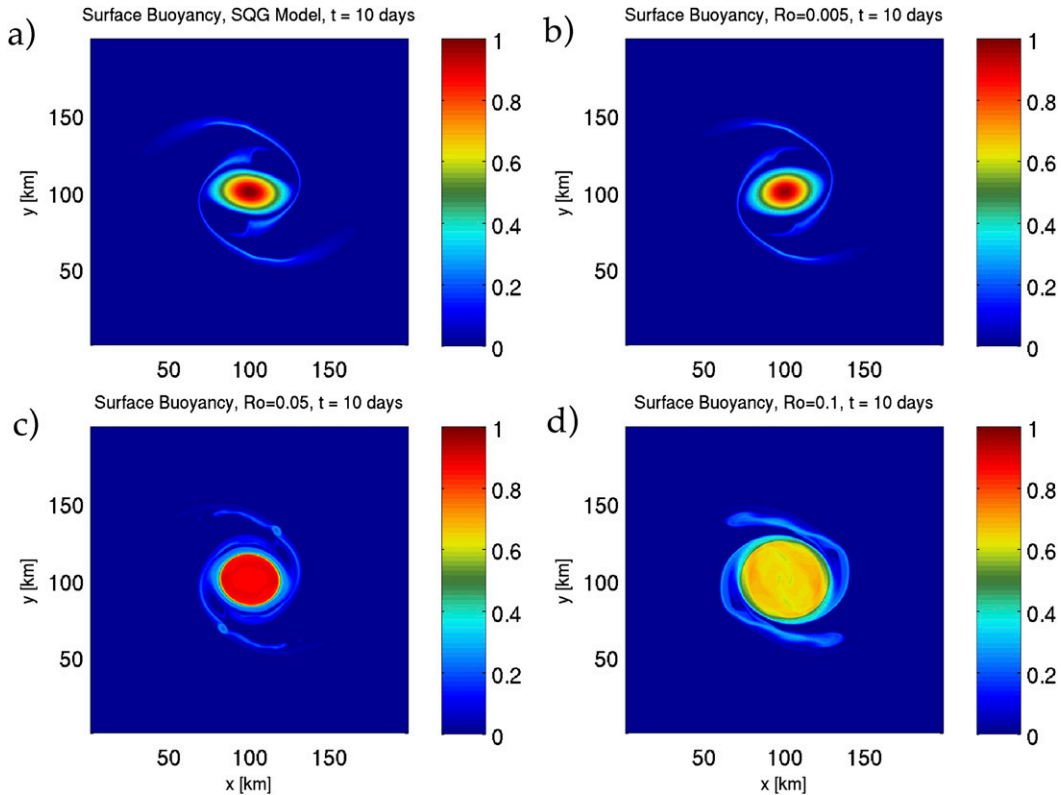
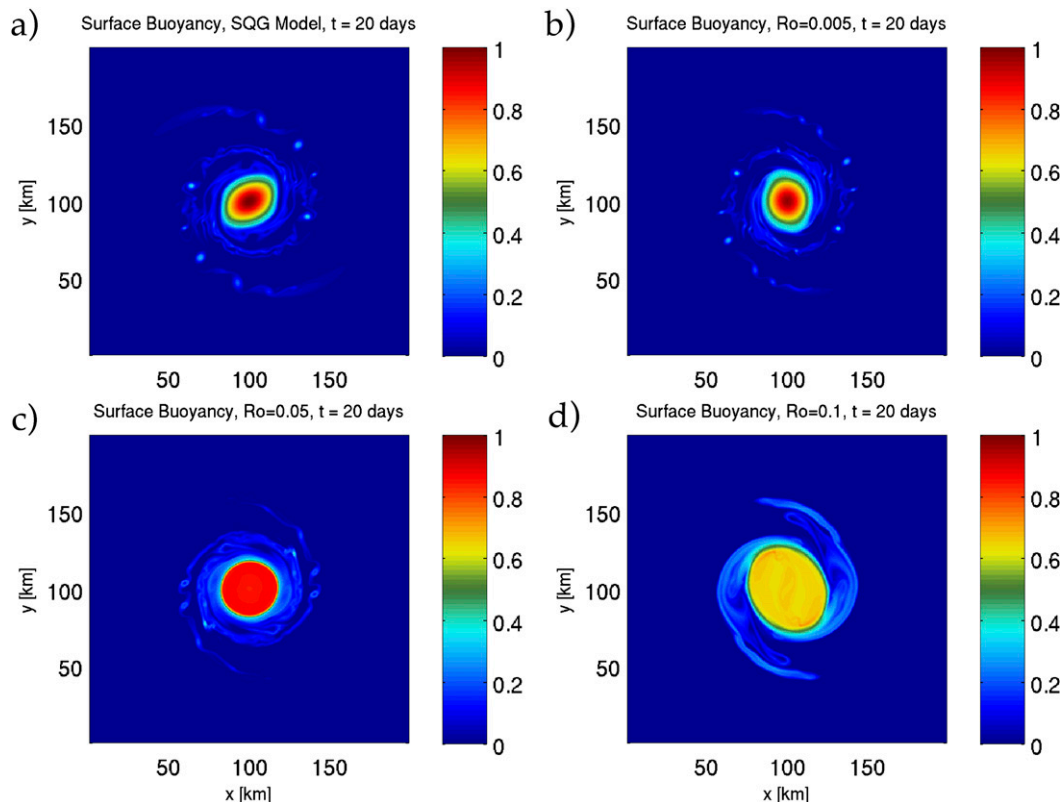


FIG. 2. Snapshots of surface buoyancy at $t = 10$ days in (a) the SQG model and in the PE model for $\text{Ro} =$ (b) 0.005, (c) 0.05, and (d) 0.1. Buoyancy fields are normalized by $b_{\text{max}} = 0.01$ m s⁻² and are plotted at $z = 0$.

FIG. 3. As in Fig. 2, but at $t = 20$.

case in Fig. 2c and is also very uniform. Again, this must be because of the effects of a stronger inertial instability in the core of the vortex. As a result of the core diverging horizontally, the amplitudes of the buoyancy fields in the cases with $Ro = 0.05$ and 0.1 have decayed significantly.

Figure 3 shows snapshots of surface buoyancy anomalies normalized by $b_{\max} = 0.01 \text{ m s}^{-2}$ after 20 days. At the later stages of evolution, we see that in the case with $Ro = 0.005$ the filaments that develop become unstable as in the SQG simulation. One difference between the two cases is that the effect of the finite Rossby number is to reduce the length and width of the filaments. As a result, there are fewer vortices that form from the secondary instability. This signifies that the filaments are stabilized as a result of an increase in Ro . In the case with $Ro = 0.05$, the filaments are even shorter and less narrow and generate far fewer and weaker secondary vortices. The $Ro = 0.1$ case shows a much larger departure from the SQG solution. In particular, no instabilities have formed on the arms of the vortex, and the core of the vortex has spread out much further than in all previous cases. While the $Ro = 0.1$ case is likely affected by the stronger filter at early times, there is a clear tendency for the arms to stabilize at later times as Ro increases from 0.005 to 0.05 to 0.1.

In our three PE simulations, the buoyancy frequency of the background state remains fixed, but the relative stratification due to the vortex changes. To illustrate how this changes in the different scenarios, in Table 3, we present the extrema of the total stratification:

$$N_{\min}^2 = N^2 + \min\left(\frac{\partial b'}{\partial z}\right), \quad \text{and} \quad (15)$$

$$N_{\max}^2 = N^2 + \max\left(\frac{\partial b'}{\partial z}\right), \quad (16)$$

in the PE solutions at $t = 0$ and 15 days. In the cases that seem to depart from the SQG solution, $Ro = 0.05$ and 0.1 , we find that regions of the fluid become destratified. Therefore, overturning is present in the mature stages of the vortex's evolution as a result of gravitational instability (e.g., Waite and Smolarkiewicz 2008).

c. Vertical vorticity

In this subsection, we investigate the evolution of vertical vorticity in the SQG and PE simulations and how it depends on the Rossby number. There are different ways of defining a Rossby number for a particular flow: while the definition in Eq. (5) uses the velocity and

TABLE 3. Computation of full stratification in the PE solutions at $t = 0$ and 15 days.

	Ro = 0.005	Ro = 0.05	Ro = 0.1
N_{\min}^2 at $t = 0$ (s^{-2})	9.66×10^{-5}	6.65×10^{-5}	3.29×10^{-5}
N_{\max}^2 at $t = 0$ (s^{-2})	1.14×10^{-4}	2.44×10^{-4}	3.87×10^{-4}
N_{\min}^2 at $t = 15$ (s^{-2})	8.75×10^{-5}	-1.46×10^{-4}	-2.15×10^{-4}
N_{\max}^2 at $t = 15$ (s^{-2})	1.29×10^{-4}	1.50×10^{-4}	1.67×10^{-4}

length scales of the initial vortex, another approach is to define a local Rossby number:

$$\text{Ro}_{\text{loc}} = \frac{\zeta}{f}, \quad (17)$$

where ζ is the vertical component of vorticity. Initially, all three cases have the local Rossby number structure at the surface, $z = 0$, shown in Fig. 4. The initial buoyancy anomaly field has a strong anticyclonic core with relatively weaker narrow cyclonic patches to the north and south of the anticyclone. The other cases have identical vortical structure with different extrema because of the different f values. The local Rossby numbers' ranges in the PE simulations are

$$\text{Ro} = 0.005: \text{Ro}_{\text{loc}} \in (-0.14, 0.02), \quad (18)$$

$$\text{Ro} = 0.05: \text{Ro}_{\text{loc}} \in (-1.4, 0.2), \quad \text{and} \quad (19)$$

$$\text{Ro} = 0.1: \text{Ro}_{\text{loc}} \in (-2.5, 0.5). \quad (20)$$

We note that the largest local Rossby numbers are approximately 30 times larger than the global Rossby number that we assigned to each case. In terms of determining whether the flow is QG or not, the local Rossby number is more relevant, but we still use the labels previously stated with the caution that they are much smaller than the local values. Given that the local Rossby numbers for the $\text{Ro} = 0.005$ simulation are all less than unity, we might expect this simulation to be very well described by SQG, and indeed this seems to be the case. By contrast, the other two cases have local Rossby numbers greater than 1 in some regions of the flow, and they both depart from SQG behavior.

Figure 5 shows the local Rossby number of the SQG solution and the three PE solutions, $\text{Ro} = 0.005, 0.05$, and 0.1 , at $t = 15$ days. We see that for the $\text{Ro} = 0.005$ case, we generate small vortical structures and increases in magnitude but are still $O(0.1)$ and therefore are consistent with the approximations of SQG. The anticyclonic core is still present at 15 days into the simulation, while the small cyclones have stretched around the core of the vortex and are barely perceptible. In the $\text{Ro} = 0.05$ and 0.1 cases, we see that the smallest features

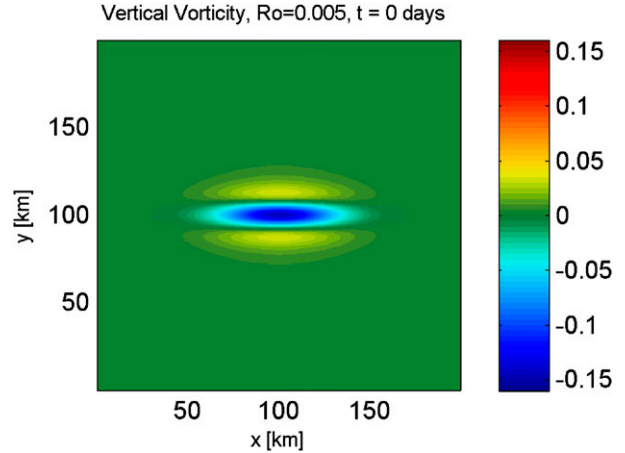


FIG. 4. Vertical vorticity, normalized by f , at $t = 0$ days and at $z = 0$ for the case with $\text{Ro} = 0.005$.

have a Rossby number $O(1)$, which does not satisfy the assumptions of SQG. The range of the local Rossby number between both these cases is very similar. As will be seen in sections 4d and 4e, the simulations with $\text{Ro} = 0.05$ and 0.1 are the only cases that generate any significant inertia-gravity waves. This is in agreement with Danioux et al. (2012) who demonstrated with their simulations that gravity waves were spontaneously generated in areas with local Rossby number at least $O(1)$ (see also Vanneste and Yavneh 2004). The central vortex, as in the case with $\text{Ro} = 0.005$, is still present in the PE solutions with $\text{Ro} = 0.05$ and 0.1 . The cyclones have stretched around the core, however, particularly in the $\text{Ro} = 0.1$ case; we can see that these cyclones have not stretched out as thinly as in the smaller Rossby number cases.

While the SQG model assumes an infinitesimal Rossby number, for the sake of comparison with the PE solutions, we can plot the local Rossby number of the SQG simulation (Fig. 5a). While the SQG local Rossby number is very similar to the PE case with $\text{Ro} = 0.005$, the magnitude of SQG structures has a Ro_{loc} 10 times the size of the Ro_{loc} in the $\text{Ro} = 0.005$ case. This is because of the different sizes of f from the SQG solution to the $\text{Ro} = 0.005$ case. We see that the SQG solution generates vortices that have a Rossby number $O(1)$ and therefore the SQG may not be able to accurately be used to describe the dynamics of these smaller vortices.

In the cases with $\text{Ro} = 0.05$ and 0.1 , we have seen that $\text{Ro}_{\text{loc}} \sim O(1)$. Physically, this signifies that even though the bulk of the flow is dominated by rotation, there are small-scale features that are not. As a result, we expect there to be significant differences between the QG and Ertel PV that originate at the small scales. Therefore, even though the QGPV is initially zero, there is no reason to expect the Ertel PV to be small. Indeed, we find

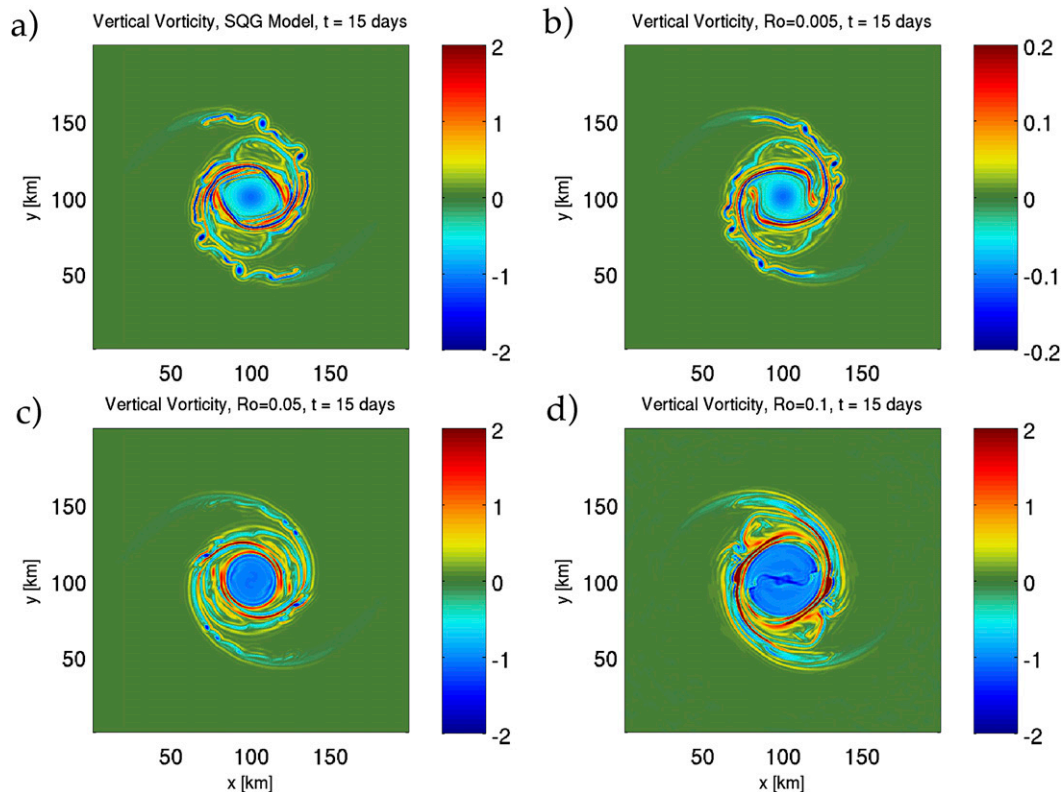


FIG. 5. Local Rossby number at $t = 15$ days for (a) the SQG solution and $Ro =$ (b) 0.005, (c) 0.05, and (d) 0.1.

significant values of Ertel PV, some negative, implying that inertial instability occurs. In both of these simulations the region where the anticyclonic fluid is strongest produces negative Ertel PV. In Fig. 6, we plot the Ertel PV ($Q = N^2\zeta + f\partial_z b' + \boldsymbol{\omega} \cdot \nabla b'$) normalized by fN^2 at $t = 0$ and 15 days for the PE cases with $Ro = 0.05$ and 0.1. Initially, the cores of these vortices have a large ellipse of negative Ertel PV, the magnitude of which increases with Ro . As the vortex evolves, we find in both cases that patches of negative Ertel PV exist in the mature state but only in very small regions on the periphery of the vortex. Vertical cross sections of Ertel PV show that it is surface trapped, as expected (not shown). Furthermore, Fig. 6 shows the emergence of positive Ertel PV in these simulations, even though the initial Ertel PV is negative. The Ertel PV is the sum of the QGPV, which is initially zero, and a small, nonlinear term. The vertical filter tends to smooth out the sharp buoyancy gradient near the surface, decreasing the magnitude of the $\partial_z b'$ term in the QGPV. In regions where $\zeta > 0$, this leads to positive QGPV and eventually positive Ertel PV, as seen in Figs. 6b and 6d.

d. Energy spectra

To further diagnose the differences between the SQG and PE simulations as a function of the Rossby number, we

examine the energy spectra. The horizontal kinetic energy in the horizontal wavenumber (k, l) can be written as

$$E(k, l, z) = \frac{1}{2}(|\hat{u}|^2 + |\hat{v}|^2) = \frac{1}{2} \left(\frac{|\hat{\zeta}|^2}{K^2} + \frac{|\hat{\delta}|^2}{K^2} \right), \quad (21)$$

where we have made the Helmholtz decomposition of the horizontal velocity. The vertical component of vorticity is $\hat{\zeta} = ik\hat{v} - il\hat{u}$, and the horizontal divergence is $\hat{\delta} = ik\hat{u} + il\hat{v}$. This decomposition allows us to calculate how much energy is in the rotational and divergent modes and is commonly used (e.g., Capet et al. 2008). Divergent energy corresponds to vertical motion and is therefore due to ageostrophic motions, including inertia-gravity waves at leading order.

Figure 7 shows kinetic energy spectra for the SQG model along with the PE simulations for Rossby numbers 0.005, 0.5, and 0.1. Since the depth between simulations changes, the depths at which we plot the energy spectra are different. However, we are plotting at the same relative depth to the depth of the vortex between simulations. In the PE solutions with $Ro = 0.005$, 0.05 and 0.1, the depths are -54 , -5.4 , and -2.7 m, respectively. The SQG solution's spectrum is computed at -5.4 m. Energy and horizontal wavenumbers have

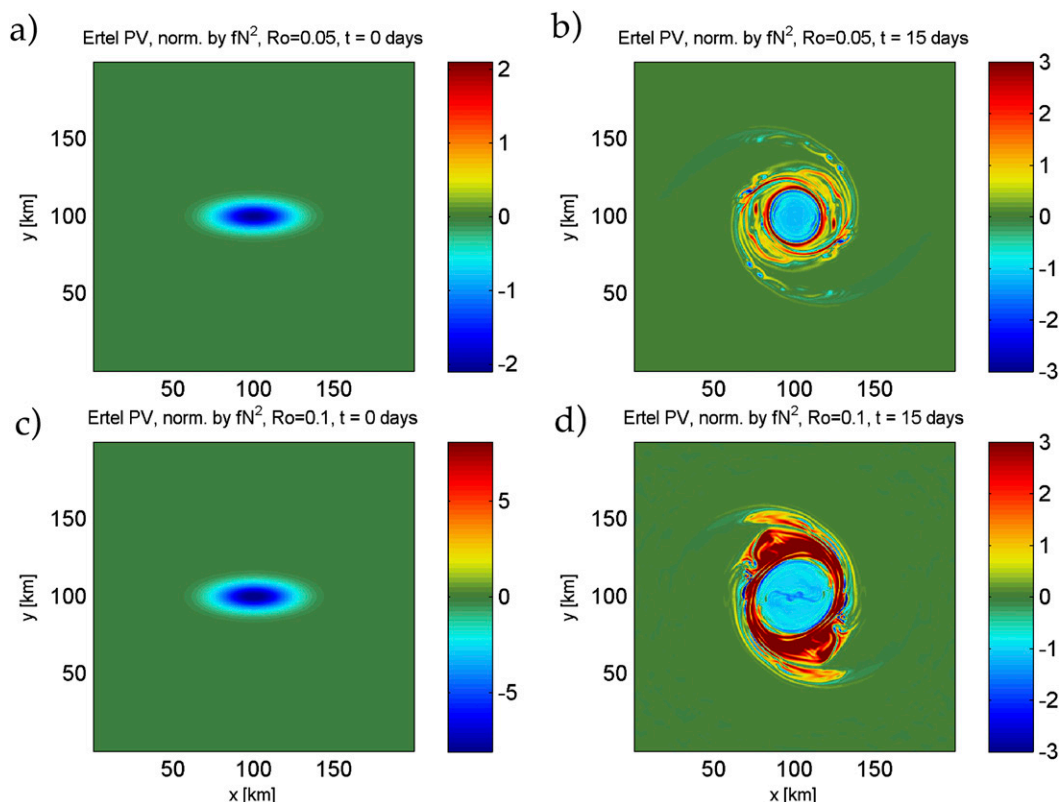


FIG. 6. Ertel PV at $t = 0$ days for $Ro =$ (a) 0.05 and (c) 0.1 and at $t = 15$ days for $Ro =$ (b) 0.05 and (d) 0.1.

been nondimensionalized by the total initial surface kinetic energy and smallest horizontal wavenumber, respectively. These spectra have been time averaged over the mature part of the simulation between 15 and 20 days where outputs were every 12 h. The total kinetic energy spectra for SQG and the PE case with $Ro = 0.005$ are almost identical, with some minor discrepancies that are likely because of the differences in the small-scale dissipation between the two numerical models. In the latter, almost all of the kinetic energy is rotational with only a very weak divergent energy spectra. The kinetic energy spectra are similar to a $K^{-5/3}$ power law that is in surprisingly good agreement with the SQG case (Pierrehumbert et al. 1994; Held et al. 1995). The similarity of the spectra is consistent with the excellent agreement between the surface buoyancy fields in the two simulations. There is a gradual increase in the steepness of the PE simulation kinetic energy spectrum as the Rossby number increases. It is also apparent that as the Rossby number increases, more energy is being transferred into the divergent modes, consistent with the generation of more gravity waves. Table 4 gives the least squares estimates of the slopes of the kinetic energy, rotational energy, and divergent energy spectra. Slopes were estimated over nondimensionalized wavenumbers

10 through 60. Here, we can easily quantify that the spectral slope is indeed increasing in steepness. Interestingly, in the cases with $Ro = 0.05$ and $Ro = 0.1$, the slope of the rotational and divergent parts of the energy spectrum are quite close.

Because of the exponential decaying profile with depth, the rotational energy also decays quickly away from the surface. As we move deeper in the fluid, we expect the divergent energy to dominate because of the presence of gravity waves that are able to propagate vertically. This is readily seen in Fig. 8 where we have plotted the logarithm of the ratio of divergent energy to rotational energy for nondimensional depth versus the nondimensional wavenumber. We can also quite clearly see that rotational energy dominates divergent energy deeper in the $Ro = 0.005$ case than in the other two cases. Figure 8 shows that at large scales, for all depths, we have that the divergent motions are much weaker than the rotational ones. However, as we move to small horizontal length scales we see that eventually the divergent motions become more important, presumably beyond the submesoscale. Indeed, the regime where this takes place grows with increasing Rossby number. Based on the agreement of the $Ro = 0.005$ case with the SQG solution, this is to be expected. The plots of the cases

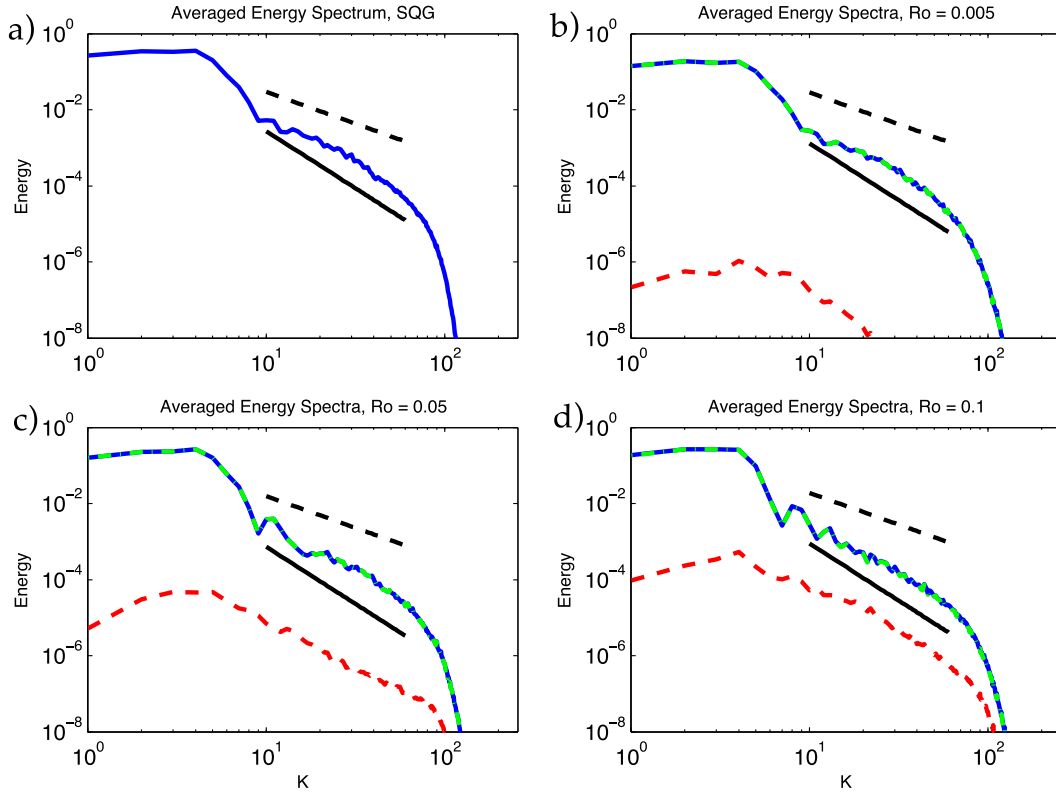


FIG. 7. Kinetic energy spectra averaged over $t = 15\text{--}20$ days for (a) the SQG model and for the PE cases with $Ro =$ (b) 0.005, (c) 0.05, and (d) 0.1. Energy is nondimensionalized by the total initial surface kinetic energy, while the horizontal wavenumber is normalized by the smallest wavenumber. Different curves correspond to kinetic energy (solid blue), rotational kinetic energy (green dashed–dotted), and divergent kinetic energy (red dash). Finally, power laws of $-5/3$ and -3 are plotted as the black dashed line and the solid black line, respectively.

with $Ro = 0.05$ and 0.1 are quite similar even though we have seen that surface dynamics are quite different. One key difference, however, is that at small scales the ratio of divergent energy to rotational energy is about two orders of magnitude larger in the $Ro = 0.1$ case compared to the $Ro = 0.05$ case. This seems to indicate that gravity waves are much stronger in the $Ro = 0.1$ case.

e. Vertical velocity and omega equation

Based on the energy spectra in Fig. 7, we expect gravity waves to be present in the PE simulations. To properly classify these, we must distinguish the vertical velocity associated with gravity waves and vertical velocity corresponding to the geostrophically balanced motion. One approach for separating these velocities is to employ the omega equation:

$$\left(N^2 \nabla_H^2 + f^2 \frac{\partial^2}{\partial z^2}\right) w = 2 \nabla \cdot \mathbf{Q}, \quad (22)$$

where

$$\mathbf{Q} = -(\nabla b_g'^{\perp} \cdot \nabla) \mathbf{u}_g^{\perp},$$

$\mathbf{u}_g^{\perp} = (-v_g, u_g)$, $\nabla b_g'^{\perp} = (-\partial_y b_g', \partial_x b_g')$, the superscript \perp indicates the orthogonal complement, and subscript g denotes geostrophic [Hoskins et al. 1978; notation follows Waite and Bartello (2006)]. Geostrophic velocities and buoyancy are computed from the pressure field in the SPINS model. When Eq. (22) is applied to a QG model, it allows us to deduce the vertical velocity in the fluid based on the assumed geostrophic and hydrostatic balances. On the other hand, when the omega equation is applied to the PE, it computes the component of vertical velocity that is believed to be due to the balanced part of the motion.

Figure 9 depicts the full vertical velocity for the PE simulations (left panels) along with the corresponding

TABLE 4. Least squares estimate of spectral slopes of horizontal kinetic energy (KE), rotational kinetic energy (RKE), and divergent kinetic energy (DKE) for SQG solution and PE solutions.

	KE	RKE	DKE
SQG	-2.72	—	—
$Ro = 0.005$	-2.72	-2.72	-4.81
$Ro = 0.05$	-2.58	-2.58	-2.37
$Ro = 0.1$	-2.68	-2.67	-2.78

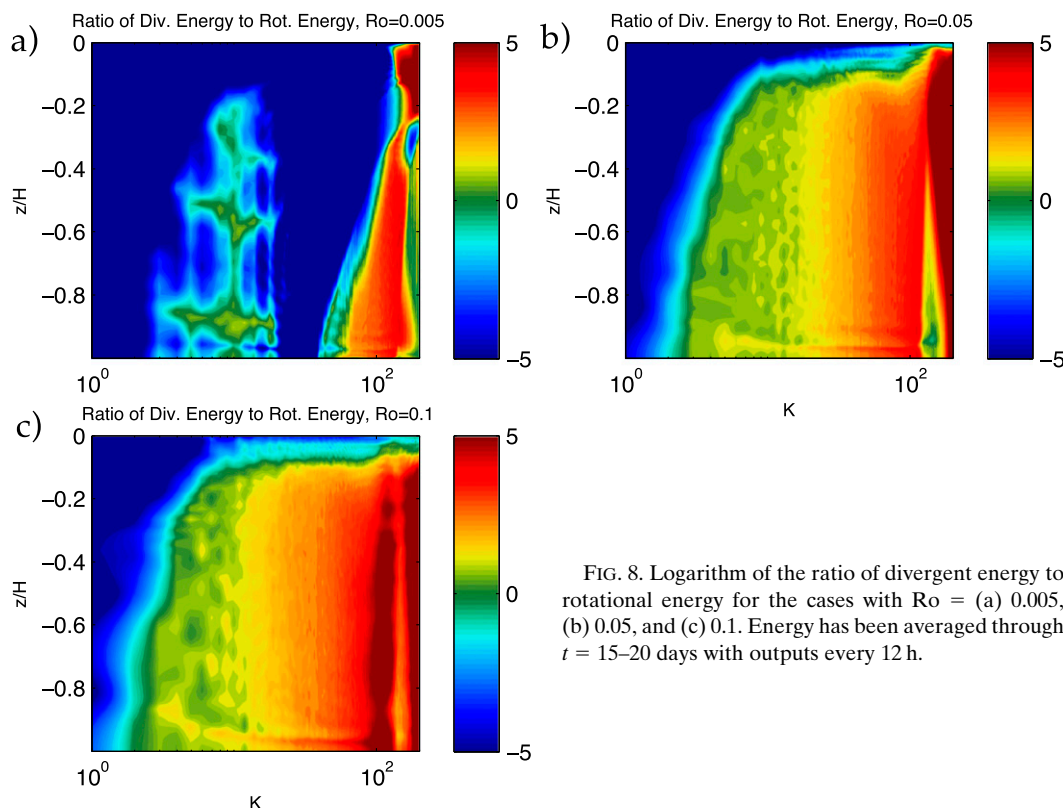


FIG. 8. Logarithm of the ratio of divergent energy to rotational energy for the cases with $Ro =$ (a) 0.005, (b) 0.05, and (c) 0.1. Energy has been averaged through $t = 15$ –20 days with outputs every 12 h.

vertical velocity from the omega equation (right panels). Velocities are normalized by 10^{-6} . The velocities are plotted at the same depth as the energy spectra discussed in section 4d of this paper. For the case with $Ro = 0.005$, the actual and omega equation vertical velocities are very similar, consistent with the agreement of this simulation with the SQG solution. As a result, we cannot see any appreciable gravity waves propagating in this case. The cases with $Ro = 0.05$ and $Ro = 0.1$ show wavelike structures in the actual vertical velocity, while the omega variable does not contain these waves. Therefore, we can see that inertia–gravity waves are being radiated away from the core of the vortex to the north and south. The wavelength of these gravity waves increases between the $Ro = 0.05$ and $Ro = 0.1$ cases. However, a separate run of $Ro = 0.05$ with identical filtering to $Ro = 0.1$ (not shown) demonstrates that this increase of wavelength is because of filtering. The dependence of wavelength on filtering strength suggests that even smaller-scale waves would be present in higher-resolution simulations. We can also see a qualitative difference in the core of the vortex. In particular, the full vertical velocity has structures within the core that are absent in the omega equation velocity. This difference might serve as an explanation as to why the core of the vortex spreads out initially in the cases with

$Ro = 0.05$ and 0.1 . A more balanced version of the initial vortex could show a decrease in the vertical motion in the core of the vortex.

Figure 10 depicts the full vertical velocity (left panels) and the vertical velocity calculated by the omega equation (right panels) for the PE simulations through the center of the y domain. As expected, the vertical velocity induced by balanced motion is surface trapped in all three cases and seems to reduce in relative size with increasing Ro . The full vertical velocity shows structures that are present at all depths of the domain that are presumably because of inertia–gravity waves. In the case with $Ro = 0.005$, large modal structures can be observed at the bottom underlying the vortex. The case with $Ro = 0.05$ is much more energetic;

In Fig. 11, we show the vertical cross section through the ellipse of the vertical velocity (left panels) and omega equation velocity (right panels) for the PE simulations through the center of the y domain. As expected, the vertical velocity induced by balanced motion is surface trapped in all three cases and seems to reduce in relative size with increasing Ro . The full vertical velocity shows structures that are present at all depths of the domain that are presumably because of inertia–gravity waves. In the case with $Ro = 0.005$, large modal structures can be observed at the bottom underlying the vortex. The case with $Ro = 0.05$ is much more energetic;

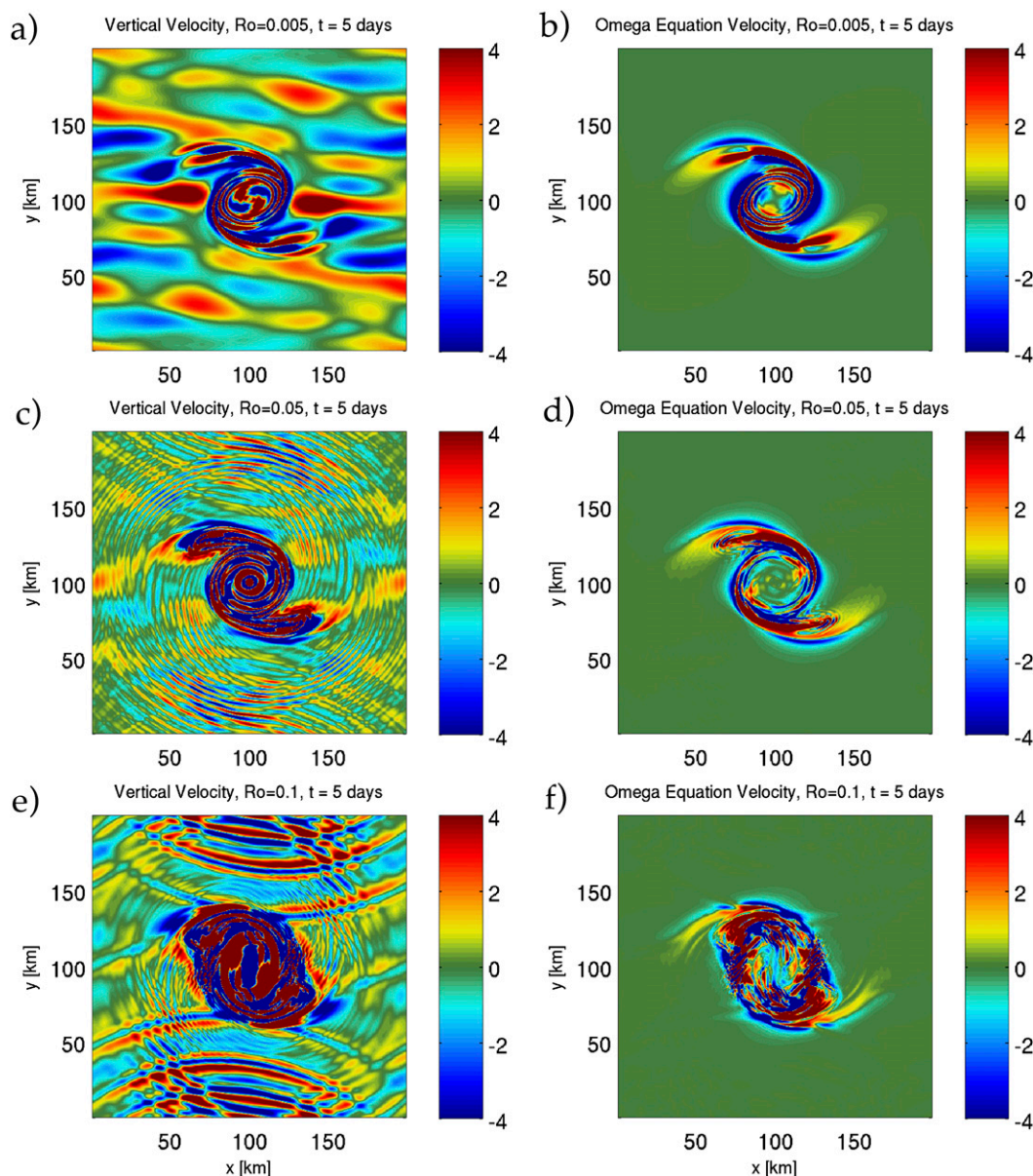


FIG. 9. (left) Vertical velocities and (right) vertical velocity induced by QG motion for the set of Rossby numbers. Velocities are normalized by 10^{-6} m s^{-1} .

it has some similar features near the bottom but also has a strong downwelling region below the vortex. The least balanced case with $Ro = 0.1$ does not have the strong downwelling region and has a clear wave pattern. These features are similar to those observed in [Kloosterziel et al. \(2007\)](#), which suggests that these structures may arise as a result of inertial instability. Similar to both of these cases is a pattern of upwelling and downwelling at the center of the vortex. The alternating bands of in the velocity field are very similar to Fig. 2 of [Joyce et al. \(2013\)](#), which presented observations of a warm-core ring obtained using a Doppler current profiler. The magnitude

of the vertical velocity in the case $Ro = 0.1$ surpasses that of the case with $Ro = 0.05$. The fact that the least balanced state yields the strongest vertical velocities is typical of submesoscale dynamics and is very important in the vertical transport of oceanic properties near the surface of the ocean ([Capet et al. 2008](#)).

5. Conclusions

In this work, we have compared the evolution of an elliptical, surface-trapped vortex using the SQG model and the nonhydrostatic Boussinesq PE. While this

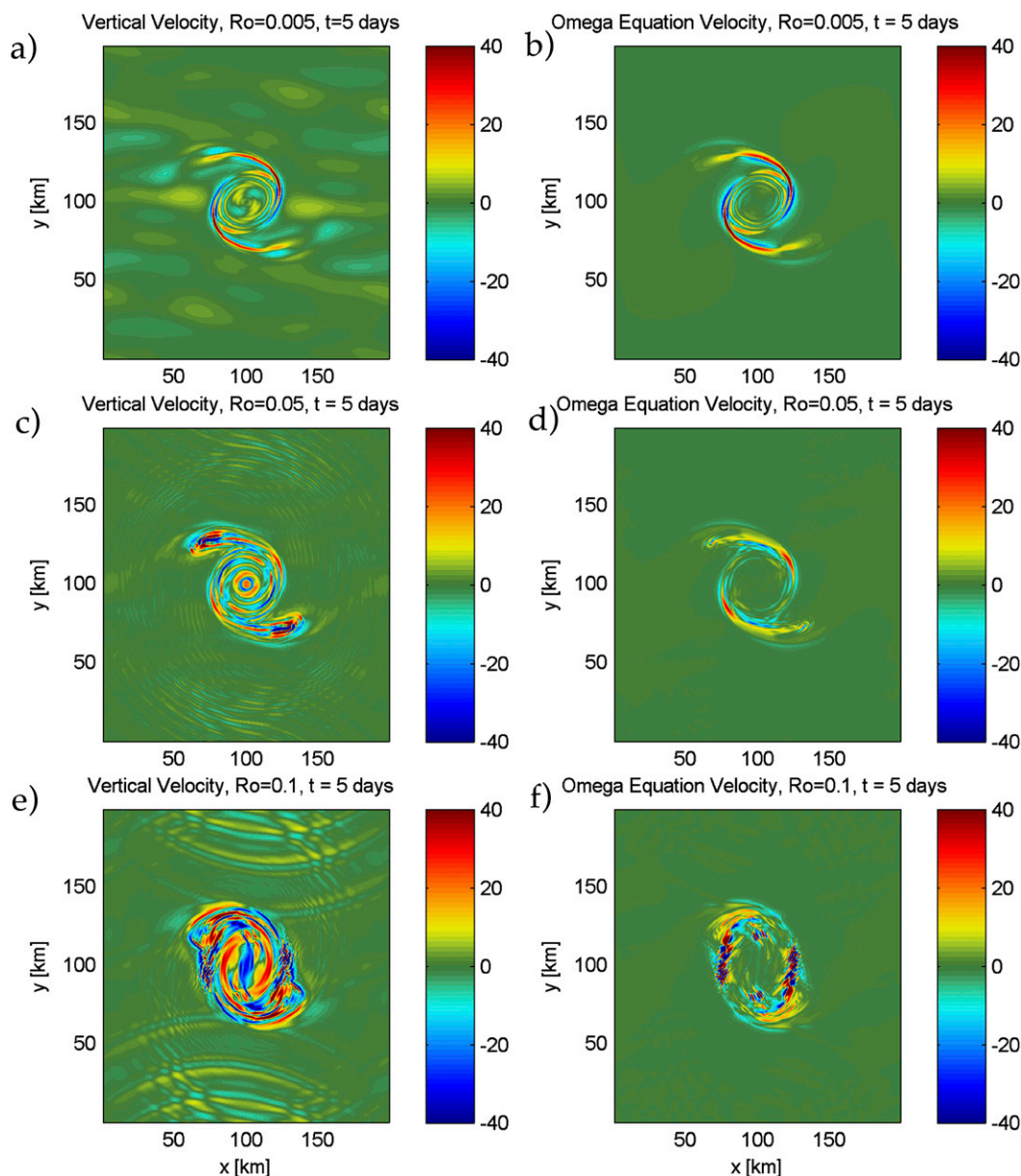


FIG. 10. As in Fig. 9, but with a larger range of w shown.

problem is of interest in its own right, it is also an ideal framework for studying the breakdown of SQG dynamics and investigating how this breakdown is manifested in the PE model. While the SQG model assumes zero interior quasigeostrophic potential vorticity, the PE model does contain nonzero initial Ertel PV. Even though the SQG approximation is a very useful model that has shed much insight into the underlying dynamics of surface-driven oceanic flows, it is important to better understand the limits of this model. From our numerical simulations, we have determined that, for sufficiently small Ro , SQG matches remarkably well with the PE, as expected. For

larger Ro , however, interesting differences between the dynamics of the two models emerge: filaments that form outside the vortex tend to widen and are more stable compared to their SQG counterparts. As a result, the secondary instabilities that form on the filaments tend to be stabilized. We expect this property applies to more general SQG flows, but further investigation is required to confirm whether this occurs in other instances. Another characteristic of non-SQG vortices is that the core of the elliptical vortex seems to mix much more easily, thereby causing the buoyancy in the core to become more uniform than what is predicted by the SQG model.

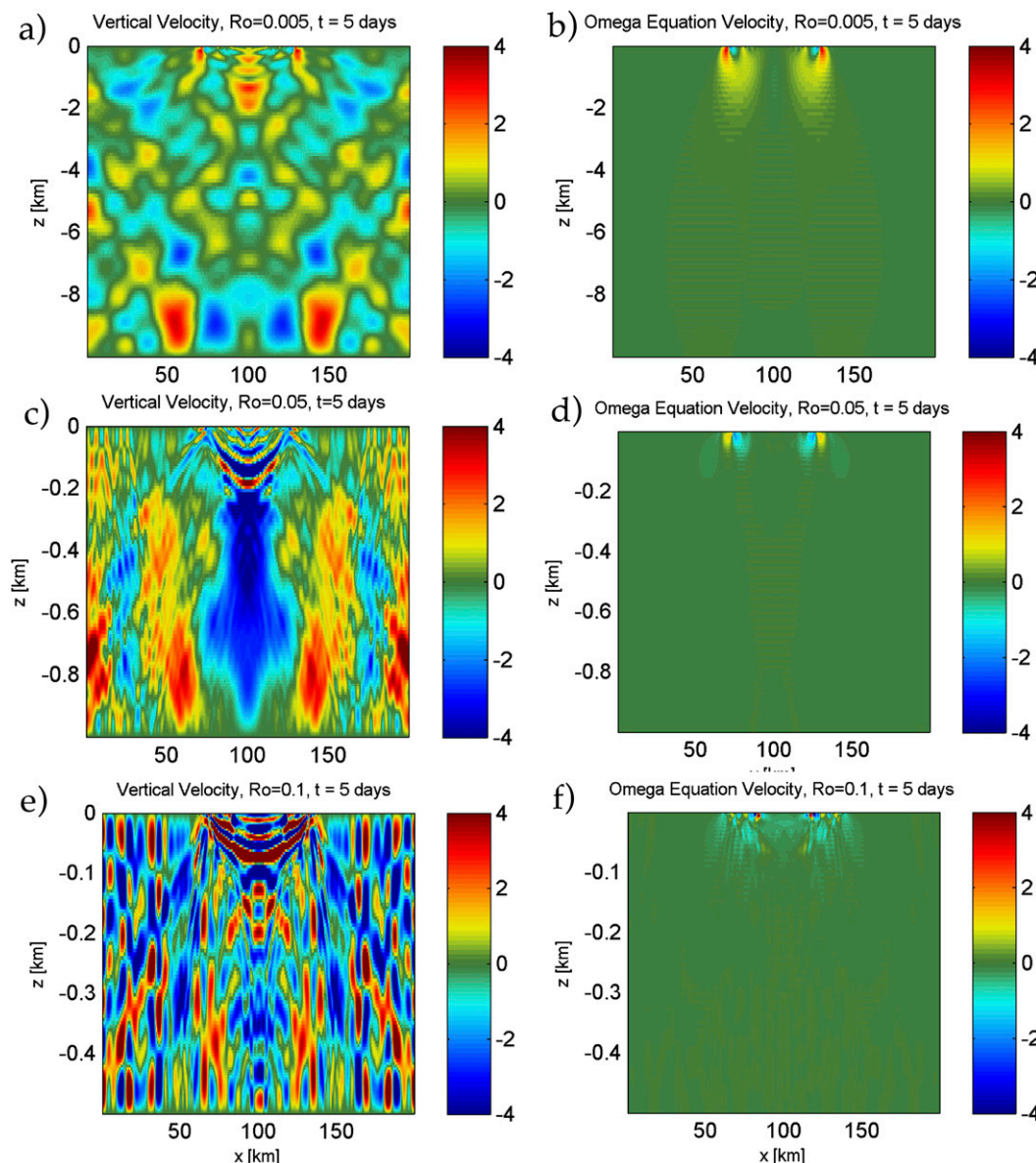


FIG. 11. Cross section through the center of the y domain of (left) vertical velocities and (right) vertical velocity induced by QG motion for the set of Rossby numbers. Velocities are normalized by 10^{-5} m s^{-1} .

For Ro defined using the length and velocity scales of the initial vortex [defined in Eq. (5)], the breakdown of SQG seems to emerge for $Ro > 0.05$. This magnitude is rather surprising as one would naively expect QG theory to hold for such a small Ro . However, when looking at the evolution of the local vorticity-based Rossby number, structures $O(1)$ develop even when the large-scale $Ro = 0.05$. This suggests that using the large-scale initial properties of the flow to estimate the relative importance of the ambient rotation can be somewhat deceptive since nonlinearities can generate locally stronger flows.

In the limit of small Ro , we have confirmed in the PE that the energy spectrum is dominated by rotational modes and that the spectral slope is similar to $-5/3$. As Ro increases and the SQG approximation breaks down, we find that the divergent part of the flow becomes increasingly more important, and this is related to the generation of inertia-gravity waves by the vortex that is due to more imbalanced initial conditions (Snyder et al. 2007). This is further enhanced by the fact that the initial elliptical vortices at larger Ro experience inertial instability. Furthermore, these two simulations also experience gravitational instabilities after they have reached a mature

state. In the case of a cyclone, we expect that the SQG results hold for larger Ro as this set of initial conditions would not be subject to inertial instabilities. However, further analysis is beyond the scope of this paper. An increase of Ro beyond the QG regime has a dichotomous effect. In the core of the vortex, we can have inertial instability whereby the core of the vortex is destabilized in the early stages of evolution. Subsequently, there is a secondary instability because of destratification in the core. In contrast, outside the vortex we have that the filaments generate fewer vortical structures, as has been previously observed in the context of barotropic shear (Poulin and Flierl 2003). Therefore, we see that in comparison to SQG dynamics, finite Ro is destabilizing in the core but stabilizing outside the vortex. The ratio of divergent to rotational energy suggests that there are submesoscale motions generated at the smallest resolved scales, and, as the Rossby number increases, this is extended down the much larger scales. Even in the nearly SQG regime we observe some submesoscale features generated near the surface, but we caution that these structures are close to the filter scale; as a result, even smaller-scale features would likely develop in even higher-resolution simulations. If one could better resolve these scales in this limit one might observe the generation of unbalanced motions even in the presence of a nearly balanced elliptical vortex.

After having investigated the dynamics of a surface-trapped elliptical vortex in some detail, there are a variety of interesting issues that can be pursued. One is to develop a more balanced version of the initial elliptical vortex and study how that structure evolves for various Rossby numbers. This approach would help to untangle if any of the observed non-SQG features are because of small imbalances in our initial conditions. Specifically, one could study the elliptical vortex in the SQG+1 model developed by Hakim et al. (2002). A second approach is to extend this model to include nonuniform stratification since that is ubiquitous in the oceans. A third would be to generalize our approach to other SQG flows, for example, a surface-trapped front, and determine whether our results extend more generally into other regimes. Clearly there is much work to be done to advance the ideas presented here, and we believe that determining the limits of SQG will only help the oceanic community to better understand for what regime parameter space it can be readily believed.

Acknowledgments. The authors thank two anonymous reviewers for their helpful comments on the manuscript, and NSERC for financial support during the research. This work was made possible by a grant from the Canadian Foundation for Innovation, and the calculations were done on the Shared Hierarchical Academic Research

Computing Network (SHARCNET; www.sharcnet.ca) and Compute/Calcul Canada.

REFERENCES

- Boyd, J., 2001: *Chebyshev and Fourier Spectral Methods*. Dover, 668 pp.
- Canuto, C., M. Y. Hussaini, A. Quarteroni, and T. A. Zang, 1988: *Spectral Methods in Fluid Mechanics*. Springer-Verlag, 374 pp.
- Capet, X., J. C. McWilliams, M. J. Molemaker, and A. F. Shchepetkin, 2008: Mesoscale to submesoscale transition in the California Current system. Part III: Energy balance and flux. *J. Phys. Oceanogr.*, **38**, 2256–2269, doi:10.1175/2008JPO3810.1.
- Carton, X., 2009: Instability of surface quasigeostrophic vortices. *J. Atmos. Sci.*, **66**, 1051–1062, doi:10.1175/2008JAS2872.1.
- Danioux, E., J. Vanneste, P. Klein, and H. Sasaki, 2012: Spontaneous inertia-gravity-wave generation by surface-intensified turbulence. *J. Fluid Mech.*, **699**, 153–173, doi:10.1017/jfm.2012.90.
- Dritschel, D. G., 2011: An exact steadily rotating surface quasigeostrophic elliptical vortex. *Geophys. Astrophys. Fluid Dyn.*, **105**, 368–376, doi:10.1080/03091929.2010.485997.
- Frigo, M., and S. G. Johnson, 2005: The design and implementation of FFTW3. *Proc. IEEE*, **93**, 216–231, doi:10.1109/JPROC.2004.840301.
- Frisius, T., 2003: The development of a cyclone–anticyclone asymmetry within a growing baroclinic wave. *J. Atmos. Sci.*, **60**, 2887–2906, doi:10.1175/1520-0469(2003)060<2887:TDOACA>2.0.CO;2.
- Hakim, G. J., C. Snyder, and D. J. Muraki, 2002: A new surface model for cyclone–anticyclone asymmetry. *J. Atmos. Sci.*, **59**, 2405–2420, doi:10.1175/1520-0469(2002)059<2405:ANSMFC>2.0.CO;2.
- Held, I. M., R. T. Pierrehumbert, S. T. Garner, and K. L. Swanson, 1995: Surface quasi-geostrophic dynamics. *J. Fluid Mech.*, **282**, 1–20, doi:10.1017/S0022112095000012.
- Hoskins, B. J., I. Draghici, and H. C. Davies, 1978: A new look at the ω -equation. *Quart. J. Roy. Meteor. Soc.*, **104**, 31–38, doi:10.1002/qj.49710443903.
- Hussaini, M. Y., D. A. Kopriva, and A. T. Patera, 1989: Spectral collocation methods. *Appl. Numer. Math.*, **5**, 177–208, doi:10.1016/0168-9274(89)90033-0.
- Joyce, T. M., J. M. Toole, P. Klein, and L. N. Thomas, 2013: A near-inertial mode observed within a Gulf Stream warm-core ring. *J. Geophys. Res. Oceans*, **118**, 1797–1806, doi:10.1002/jgrc.20141.
- Juckes, M., 1994: Quasigeostrophic dynamics of the tropopause. *J. Atmos. Sci.*, **51**, 2756–2768, doi:10.1175/1520-0469(1994)051<2756:QDOTT>2.0.CO;2.
- Klein, P., B.-L. Hua, G. Lapeyre, X. Capet, S. Le Gentil, and H. Sasaki, 2008: Upper ocean turbulence from high-resolution 3D simulations. *J. Phys. Oceanogr.*, **38**, 1748–1763, doi:10.1175/2007JPO3773.1.
- Kloosterziel, R. C., G. F. Carnevale, and P. Orlandi, 2007: Inertial instability in rotating and stratified fluids: Barotropic vortices. *J. Fluid Mech.*, **583**, 379–412, doi:10.1017/S0022112007006325.
- Kundu, P. K., and I. M. Cohen, 2010: *Fluid Mechanics*. Academic Press, 904 pp.
- LaCasce, J. H., 1998: A geostrophic vortex over a slope. *J. Phys. Oceanogr.*, **28**, 2362–2381, doi:10.1175/1520-0485(1998)028<2362:AGVOAS>2.0.CO;2.
- , 2012: Surface quasigeostrophic solutions and baroclinic modes with exponential stratification. *J. Phys. Oceanogr.*, **42**, 569–580, doi:10.1175/JPO-D-11-0111.1.

- , and A. Mahadevan, 2006: Estimating subsurface horizontal and vertical velocities from sea-surface temperature. *J. Mar. Res.*, **64**, 695–721, doi:[10.1357/002224006779367267](https://doi.org/10.1357/002224006779367267).
- Lapeyre, G., and P. Klein, 2006: Dynamics of the upper oceanic layers in terms of surface quasigeostrophy theory. *J. Phys. Oceanogr.*, **36**, 165–176, doi:[10.1175/JPO2840.1](https://doi.org/10.1175/JPO2840.1).
- Le Traon, P. Y., P. Klein, B.-L. Hua, and G. Dibarboure, 2008: Do altimeter wavenumber spectra agree with the interior or surface quasigeostrophic theory? *J. Phys. Oceanogr.*, **38**, 1137–1142, doi:[10.1175/2007JPO3806.1](https://doi.org/10.1175/2007JPO3806.1).
- Molemaker, M. J., J. C. McWilliams, and X. Capet, 2010: Balance and unbalanced routes to dissipation in an equilibrated Eady flow. *J. Fluid Mech.*, **654**, 35–63, doi:[10.1017/S0022112009993272](https://doi.org/10.1017/S0022112009993272).
- Nastrom, G. D., and K. S. Gage, 1985: A climatology of atmospheric wavenumber spectra of wind and temperature observed by commercial aircraft. *J. Atmos. Sci.*, **42**, 950–960, doi:[10.1175/1520-0469\(1985\)042<0950:ACOAWS>2.0.CO;2](https://doi.org/10.1175/1520-0469(1985)042<0950:ACOAWS>2.0.CO;2).
- Pierrehumbert, R. T., I. M. Held, and K. L. Swanson, 1994: Spectra of local and nonlocal two-dimensional turbulence. *Chaos Solitons Fractals*, **4**, 1111–1116, doi:[10.1016/0960-0779\(94\)90140-6](https://doi.org/10.1016/0960-0779(94)90140-6).
- Poulin, F. J., and G. R. Flierl, 2003: The nonlinear evolution of barotropically unstable jets. *J. Phys. Oceanogr.*, **33**, 2173–2192, doi:[10.1175/1520-0485\(2003\)033<2173:TNEOBU>2.0.CO;2](https://doi.org/10.1175/1520-0485(2003)033<2173:TNEOBU>2.0.CO;2).
- Snyder, C., D. J. Muraki, R. Plougonven, and F. Zhang, 2007: Inertia-gravity waves generated within a dipole vortex. *J. Atmos. Sci.*, **64**, 4417–4431, doi:[10.1175/2007JAS2351.1](https://doi.org/10.1175/2007JAS2351.1).
- Subich, C. J., K. G. Lamb, and M. Stastna, 2013: Simulation of the Navier–Stokes equations in three dimensions with a spectral collocation method. *Int. J. Numer. Methods Fluids*, **73**, 103–129, doi:[10.1002/fld.3788](https://doi.org/10.1002/fld.3788).
- Trefethen, L. N., 2000: *Spectral Methods in MATLAB*. SIAM, 165 pp.
- Tulloch, R., and K. S. Smith, 2006: A new theory for the atmospheric energy spectrum: Depth-limited temperature anomalies at the tropopause. *Proc. Natl. Acad. Sci. USA*, **103**, 14 690–14 694, doi:[10.1073/pnas.0605494103](https://doi.org/10.1073/pnas.0605494103).
- , and —, 2009: Quasigeostrophic turbulence with explicit surface dynamics: Application to the atmospheric energy spectrum. *J. Atmos. Sci.*, **66**, 450–467, doi:[10.1175/2008JAS2653.1](https://doi.org/10.1175/2008JAS2653.1).
- Vallis, G. K., 2006: *Atmospheric and Oceanic Fluid Dynamics: Fundamentals and Large-Scale Circulation*. Cambridge University Press, 745 pp.
- Vanneste, J., and I. Yavneh, 2004: Exponentially small inertia-gravity waves and the breakdown of quasigeostrophic balance. *J. Atmos. Sci.*, **61**, 211–223, doi:[10.1175/1520-0469\(2004\)061<0211:ESIWAT>2.0.CO;2](https://doi.org/10.1175/1520-0469(2004)061<0211:ESIWAT>2.0.CO;2).
- Waite, M. L., and P. Bartello, 2006: The transition from geostrophic to stratified turbulence. *J. Fluid Mech.*, **568**, 89–108, doi:[10.1017/S0022112006002060](https://doi.org/10.1017/S0022112006002060).
- , and P. K. Smolarkiewicz, 2008: Instability and breakdown of a vertical vortex pair in a strongly stratified fluid. *J. Fluid Mech.*, **606**, 239–273, doi:[10.1017/S0022112008001912](https://doi.org/10.1017/S0022112008001912).
- Whitaker, J., 1993: A comparison of primitive and balance equation simulations of baroclinic waves. *J. Atmos. Sci.*, **50**, 1519–1530, doi:[10.1175/1520-0469\(1993\)050<1519:ACOPAB>2.0.CO;2](https://doi.org/10.1175/1520-0469(1993)050<1519:ACOPAB>2.0.CO;2).